Litton
TASC

TIM-08336-0B-0S-02

Concept Discussion for Laser Detection of Local Atmospheric Particle Motion Generated by Turbulence

8 April 1999

Prepared for:

VOLPE NATIONAL TRANSPORTATION SYSTEMS CENTER
55 Broadway, Kendall Square
Cambridge, Massachusetts 02142

under:

Contract No. DTRS-57-93-D-00072
Functional Area CNS
TTD CB5217

Prepared by:
Todd M. Freyman
Charles L. Medler
Peter B. Morris
Jack Oswald

Approved by:
Ellen B. Meadors

Table of Contents

List of Tables

List of Figures

Table of Symbols

λ	Acoustic wavelength (m)
γ	Ratio of specific heats (C_p/C_v)
Φ	Total or average radiant power (W)
ρ	Air density (kg/m^3)
ρ_0	Stagnation density (kg/m^3)
σ_{CR}	Cramer-Rao lower bound error variance
ΔD	Distance over which laser energy is received over the gate interval (m)
φ_{eddy}	Phase shift associated with eddy motion (rad)
λ_L	Laser wavelength (m)
λ_{Lr}	Received laser wavelength (m)
λ_{Lref}	Reflected laser wavelength (m)
a	Atmospheric attenuation coefficient (dB/m)
A	Area (m^2)
A_a	Acoustic attenuation due to atmospheric energy absorption (dB)
A_{ab}	Broadband acoustic attenuation (dB)
A_e	Acoustic attenuation due to excess attenuation (dB)
A_s	Acoustic attenuation due to geometric spreading (dB)
A_T	Total acoustic attenuation (dB)
b_0	Laser beam diameter (m)
c	Speed of light (m/s)
c_p	Specific heat at constant pressure (J/(kg·K))
c_v	Specific heat at constant volume (J/(kg·K))
f	Acoustic frequency (Hz)
f_0	Focal length (m)
f_{eddy}	Eddy frequency (Hz)
f_L	Laser frequency (Hz)
f_{Lr}	Received laser frequency (Hz)
f_{rN}	Vibrational relaxation frequency for nitrogen (Hz)
f_{rO}	Vibrational relaxation frequency for oxygen (Hz)

g	Geometric attenuation factor
h	Molar concentration of water vapor (%)
h_{rel}	Relative humidity (%)
M	Number of data point used in power spectral density estimates
m	Particle mass (kg)
MPE	Maximum Permissible Exposure (J/cm^2 or W/cm^2)
n	Number of distinct estimates of the power spectral density
P_0	Stagnation pressure (Pa)
p_a	Ambient atmospheric pressure (Pa)
P_{max}	Maximum acoustic pressure (Pa)
P_{min}	Minimum acoustic pressure (Pa)
p_r	Reference atmospheric pressure (Pa)
P_{RMS}	Root mean square pressure (Pa)
P_S	Static pressure (Pa)
p_{sat}	Saturation vapor pressure (Pa)
R	Ideal gas constant (J/(kg·K))
r	Radius (m)
r_{NOHD}	Nominal hazard distance (m)
s	Displacement (m)
SPL	Sound Pressure Level (decibels, dB)
T	Temperature (K)
t	time (s)
T_0	Lidar gate start time (s)
T_G	Lidar gate time (s)
T_P	Lidar pulse width (s)
T_r	Reference atmospheric temperature (K)
u	Air molecule velocity (m/s)
V	Relative velocity between air molecules and particle (m/s)
$V_{acoustic}$	Line-of-sight acoustic air molecule velocity (m/s)
V_D	Velocity difference between lidar and particle (m/s)
V_{eddy}	Line-of-sight turbulent eddy velocity (m/s)

V_{lidar}	Lidar system velocity (m/s)
$V_{particle}$	Line-of-sight particle velocity (m/s)
v_s	Speed of sound (m/s)
V_{wind}	Line-of-sight wind velocity (m/s)
x	Position (m)

1. INTRODUCTION

The aviation industry can improve safety by providing pilots with information to avoid or prepare for flight through turbulence hazards. A turbulence detection system with a high detection probability and very low false alarm rate has yet to be developed. Acoustic sensing systems have been shown to be capable of detecting turbulence-generated infrasound. Lidar systems have been employed to detect particle motion induced by turbulence. Both of these techniques can be utilized to detect the presence of turbulence. However, neither sufficiently meets the needs of the aviation industry to detect flight path turbulence and provide the flight crew or ground controllers with sufficient forewarning.

Infrasound detection systems generally consist of an array of four or more microphones at ground level in conjunction with various space filtering techniques to minimize the effects of local turbulent wind eddies. The infrasound signals from the microphones are analyzed to resolve both the sound pressure level and source direction. Studies have shown good correlation between received infrasound and evidence of turbulence such as pilot reports, weather service tracking of storms and radiosonde data.

Lidar systems have been applied to remotely detect wind velocities since 1966. Lidar illuminates particles in the atmosphere with a laser and monitors the light backscattered from the particles for a shift in wavelength from that of the laser. The observed wavelength shift, called a Doppler shift, is proportional to the relative velocity difference between the lidar unit and the particles. The assumption is made that the particles are light and are entrained in the flow field to be measured. Thus, the velocity of the air molecules can be determined through analysis of the Doppler shift.

In Chapter 2 of this report, reviews the underlying physics and Doppler lidar technologies that are essential for analyzing any lidar-based system for detecting turbulence via its acoustic emanations. Chapter 3 discusses particle motion induced by turbulence generated acoustic waves and other atmospheric motion. The fundamentals of the most basic concept for detecting turbulence via its acoustic emanations, i.e., processing data from a single lidar beam intercepting an existing acoustic wave, are discussed in Chapter 4. Finally, Chapter 5 summarizes identified challenges confronting the development and application of a Doppler lidar system for the acoustic detection of turbulence.

2. PHYSICS AND TECHNOLOGY REVIEW

This chapter provides a concise review of the physics and technology associated with laser detection of particle motion induced by turbulence-generated acoustic waves. The review forms a foundation to support the assumptions and analysis in subsequent chapters.

2.1 Acoustics

Sound waves travel through a gaseous medium such as the atmosphere as a series of alternating compression and rarefaction waves. The sound pressure level (SPL) is a measure of the root mean square (RMS) pressure fluctuation. Sound pressure levels are usually expressed on a logarithmic scale in units of decibels (dB) due to the very large range of sound pressures. The decibel represents a ratio of the RMS pressure in the sound wave to a reference pressure as shown in Equation 2.1 where P_{RMS} is the RMS pressure in Pascals. Reference pressure is commonly set at the minimum threshold of human hearing for a 1,000 Hz pure tone, 20 μPa.

$$\text{SPL (dB)} = 20\log_{10}\left(\frac{P_{RMS}}{20\times10^{-6}\,Pa}\right) \qquad \text{Eq. 2.1}$$

The audible frequency range for human hearing is from about 20 Hz up to 20,000 Hz. Very low frequencies, those below 20 Hz, are termed 'infrasound' and can carry for long distances through the atmosphere due to low attenuation and channeling effects.[6] Sound waves do not induce any net motion of the air molecules in the medium but rather the air molecules respond to the passage of the waves by oscillating. For infrasound, the oscillation amplitude of the air molecules is much smaller than the wavelength. For example, a 1,000 Hz sound wave at a sound pressure level of 120 dB has a wavelength of 34 cm while the oscillation amplitude of the air molecules is only 11 μm. The pressure, density and air molecule velocity oscillate 90 degrees out of phase with the air molecule displacement as illustrated by the graph in Figure 2.1. The oscillation frequency is driven by the acoustic source and is directly related to the wavelength as shown in Equation 2.2 where f is the frequency in Hertz (Hz, 1/s), v_s is the speed of sound in meters per second and λ is the wavelength in meters.

$$f = \frac{v_s}{\lambda} \qquad \text{Eq. 2.2}$$

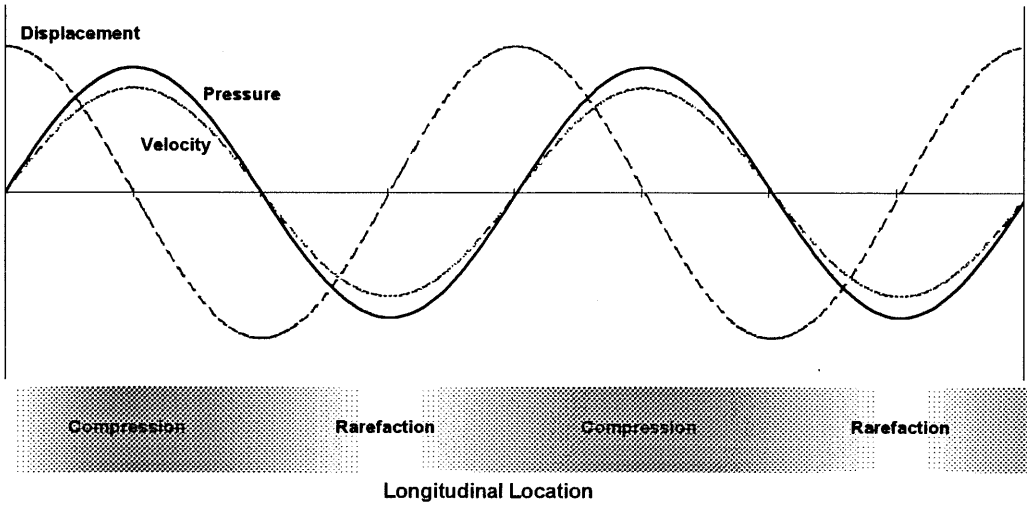

Figure 2.1 Sound Wave Characteristics

2.1.1 *Infrasound Produced by Turbulence*

Turbulence phenomenon present in the atmosphere radiate acoustic waves.[13] A very limited amount of data on acoustic emanation from atmospheric turbulence has been acquired. Sources of turbulence include naturally occurring meteorological phenomenon such as storms, thermals, convective gusts, vertical wind shear, frontal boundaries and gravity/shear waves as well as man-made disturbances such as aircraft wake vortices.

Storms and frontal boundaries most often are accompanied by clouds which provide visible indications of the potential for turbulence. Open air turbulent disturbances in the absence of clouds are referred to as clear air turbulence (CAT) due to the lack of a visually observable signature. Most CAT and even some turbulent motions near the ground occur when shear exceeds a critical point. Shear flows with characteristics beyond the critical point exhibit shear instability and spontaneously develop wavelike undulations called shear-induced turbulence. The shear-induced turbulence generation mechanism is illustrated in Figure 2.2.

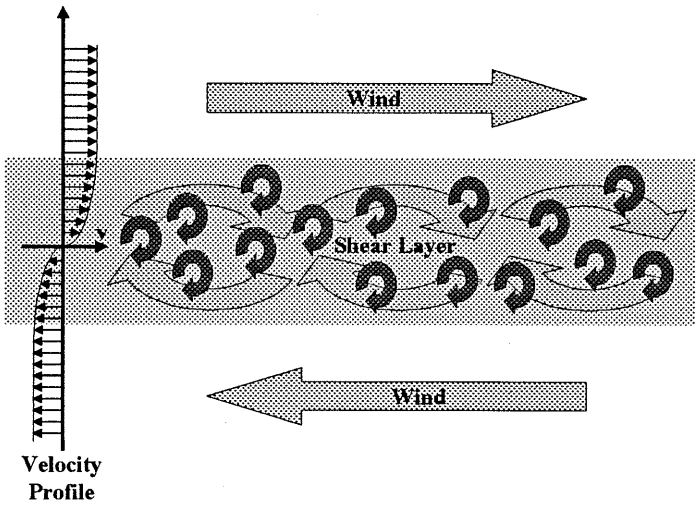

Figure 2.2 Shear-Induced Turbulence Mechanism

The majority of turbulence studies have concentrated on measuring turbulent static pressure fluctuations directly rather than the acoustic waves they emanate. However, several studies performed by NOAA have investigated acoustic wave emanation from turbulence. Bedard correlated turbulence encounter reports from aircraft flying over the continental divide in Colorado with infrasound measurements made from an array of infrasonic microphones. Data analysis lead to the conclusion that both temporal and spatial relationships between the measured infrasound and the aircraft turbulence reports existed, i.e., the infrasound that was observed was very likely generated by the turbulence encountered by the aircraft.[1,2] Khalaf and Stoughton measured acoustic waves from hurricane Diana in September 1984 at 85dB when the eye was 200 miles from the ground-level acoustic microphone array.[15] Crocker and Posmentier have also reported on acoustic emanation from turbulence.[6,24] Table 2.1 summarizes the information collected on turbulence related acoustic waves.

Table 2.1 Infrasound Produced by Turbulence[6,15,24]

Source	Frequency	Sound Pressure Level	Mechanism	Source Altitude
Mountain Waves[6]	0.02 – 0.1 Hz	74 – 104 dB	Wind flow over mountain ridges	Surface to 4 km
Severe Storms[6]	0.02 – 10 Hz	68 – 84 dB @ 30 – 800 km	Convection and wind shear	Surface to 11 km
Hurricane[15]	1 – 10 Hz	85 dB @ 322 km	Convection and wind shear	Surface to 11 km
Clear Air Turbulence[24]	1 – 16 Hz	79 – 86 dB	Wind shear	Variable

2.1.2 *Infrasound Noise Sources*

In addition to the infrasound radiated by turbulence phenomenon, numerous other natural and man-made sources exist. Since the goal is to detect turbulence, these other infrasound sources are necessarily considered background noise. Natural sources include avalanches, volcanoes, earthquakes, nonlinear interaction of ocean waves, meteors and aural motion. Noise sources added to the environment by humans includes large explosions, rocket launches and reentry and supersonic flight. Table 2.2 shows some examples of acoustic noise sources and their characteristics.

For an aircraft based detection system, any infrasound generated by the aircraft will also act as a source of noise. During flight, pressure forces induce bending moments on the airframe which responds by flexing. The flexing motion can result in oscillations in the infrasound region. For example, Boeing 777-200/300 and Airbus A330 and A340 aircraft exhibit fuselage resonation in the 2 – 3 Hz range.[37]

Table 2.2 Infrasound Noise Sources[6]

Noise Source	Frequency	Sound Pressure Level	Mechanism	Source Altitude
Microbaroms	0.125 – 0.5 Hz	54 – 94 dB	Nonlinear interaction of ocean waves	Sea Level
Aurora	0.01 – 0.1 Hz	74 – 88 dB	Supersonic motion of auroral arc	> 100 km
Meteors	0.06 – 5 Hz	68 – 94 dB @ 200 – 1,200 km	Explosive interaction with atmosphere	> 25 km
Avalanches	0.5 – 2 Hz	60 – 68 dB @ 100 km	Leading-edge roll of avalanche	Surface
Volcanoes	< 0.01 Hz	118 dB @ 10,000 km	High-energy compression of atmosphere	Surface to 10 km
Earthquakes	0.03 – 0.125 Hz	74 – 100 dB	Ground motion at epicenter	Surface

2.1.3 *Propagation*

The propagation of an acoustic wave is characterized by the propagation speed and the decay in sound pressure level over distance. The speed at which acoustic waves propagate through the atmosphere, i.e., the speed of sound, can be calculated as a function of temperature as shown in Equation 2.3 where v_s is the speed of sound in m/s, γ is the specific heat ratio ($\gamma = 1.4$ for air), R is the ideal gas constant ($R = 287$ J/kg/K) and T is the temperature in degrees Kelvin. Because the temperature of the atmosphere varies with altitude, the speed of sound varies as well. Through the troposphere, the speed of

sound decreases linearly from approximately 340 m/s at sea level to 295 m/s at 11 km, i.e., the nominal top of the troposphere.

$$v_s = \sqrt{\gamma RT} \qquad \text{Eq. 2.3}$$

Sound pressure level decay occurs due to geometric spreading, A_s, atmospheric energy absorption, A_a and 'excess' attenuation, A_e. The sum of these three factors yields the total attenuation, A_T, in dB as shown in Equation 2.4.

$$A_T = A_s + A_a + A_e \qquad \text{Eq. 2.4}$$

Geometric spreading acts to decrease the sound pressure level as the acoustic energy propagates away from the source, dispersing the emanated energy over a volume that continuously increases with distance from the source. This effect can be modeled using Equation 2.5 where As is the geometric spreading attenuation in dB, r_2 is the distance between the receiver and the center of the acoustic source, r_1 is the distance between the known sound pressure level location and the center of the acoustic source and g is a geometric factor that is assigned to zero for plane wave propagation, ½ for cylindrical propagation and 1 for spherical wave propagation.

$$A_s = 20g\log_{10}\left(\frac{r_2}{r_1}\right) \qquad \text{Eq. 2.5}$$

Atmospheric attenuation of acoustic energy results from heat conduction and shear viscosity losses and molecular relaxation losses associated with energy exchange between molecular translation and molecular vibration and rotation. These losses are typically expressed as the atmospheric attenuation coefficient, a, in decibels per meter. Subsequently, the atmospheric attenuation, A_a, can be calculated using Equation 2.6 where r is the distance from the source in meters.[6]

$$A_a = ar \qquad \text{Eq. 2.6}$$

The atmospheric attenuation coefficient, a, varies as a function of acoustic frequency, temperature and humidity. The coefficient can be calculated via the following series of equations. First, the attenuation coefficient for a pure tone is determined using Equation 2.7 where f is the acoustic frequency in Hz, p_a is the ambient atmospheric pressure in kilopascals (kPa), p_r is the reference atmospheric pressure equal to 101.325 kPa, T_r is the reference temperature equal to 293.15 K, T is the ambient atmospheric temperature in kelvin, f_{rO} is the vibrational relaxation frequency for oxygen in Hz and f_{rN} is the vibrational relaxation frequency for nitrogen in Hz.[6]

$$a = 8.686 f^2 \left(\left[1.84 \times 10^{-11} \left(\frac{p_a}{p_r} \right)^{-1} \left(\frac{T}{T_r} \right)^{1/2} \right] + \left(\frac{T}{T_r} \right)^{-5/2} \left\{ 0.01275 \left[\exp\left(\frac{-2239.1}{T} \right) \right] \left[\frac{f_{rO}}{f_{rO}^2 + f^2} \right] \right.\right.$$

$$\left.\left. + 0.1068 \left[\exp\left(\frac{-3352.0}{T} \right) \right] \left[\frac{f_{rN}}{f_{rN}^2 + f^2} \right] \right\} \right) \qquad \text{Eq. 2.7}$$

The vibrational relaxation frequencies of oxygen and nitrogen can be calculated using equations 2.8 and 2.9 where h is the molar concentration of water vapor in percent and the other variables are the same as in Equation 2.7.[6,38]

$$f_{rO} = \frac{p_a}{p_r} \left\{ 24 + \left[\frac{\left(4.04 \times 10^4 h\right)\left(0.02 + h\right)}{0.391 + h} \right] \right\} \qquad \text{Eq. 2.8}$$

$$f_{rN} = \frac{p_a}{p_r} \left(\frac{T}{T_r} \right)^{-1/2} \left(9 + 280 h \exp\left\{ -4.170 \left[\left(\frac{T}{T_r} \right)^{-1/3} - 1 \right] \right\} \right) \qquad \text{Eq. 2.9}$$

Since atmospheric water concentration is typically given as relative humidity, the molar concentration can be calculated using Equation 2.10 where h_{rel} is the relative humidity in percent, p_{sat}/p_r is the ratio of the saturation vapor pressure to the relative vapor pressure, p_a is the ambient atmospheric pressure in kPa and p_r is the reference atmospheric pressure equal to 101.325 kPa. The ratio of the saturation vapor pressure to the relative vapor pressure can be closely approximated using Equation 2.11 where T is the ambient temperature in kelvin.[6,38]

$$h = h_{rel} \left(\frac{p_{sat}}{p_r} \right) \left(\frac{p_a}{p_r} \right)^{-1} \qquad \text{Eq. 2.10}$$

$$\frac{p_{sat}}{p_r} = 10^{\left(-6.8346 \left(\frac{273.16}{T} \right)^{1.261} + 4.6151 \right)} \qquad \text{Eq. 2.11}$$

Broadband acoustic wave attenuation is normally less than that of pure tones. Based on the midband frequency of a broadband acoustic wave, the atmospheric attenuation can be closely approximated for a one-third octave band of noise using Equation 2.12 where A_{ab} is the broadband attenuation in dB and A_T is the total pure tone attenuation at the midband frequency in dB.[6]

$$A_{ab} = A_T \left(1 + 0.00533 \left[1 - 0.2303 A_T\right]\right)^{1.6} \qquad \text{Eq. 2.12}$$

Other attenuation components exist and are collectively referred to as 'excess' attenuation. These components include the ground, foliage and buildings. These effects are assumed negligible to avoid venturing into a realm of greatly increased complexity. Thus, the results of this study will be confined to the underlying assumption of operation in an uncluttered environment.

2.1.4 *Channels*

Infrasound propagates over long distances due to minimal attenuation by the atmosphere at infrasound frequencies and due to strong naturally occurring refracting channels in the atmosphere. The refracting channels are formed by vertical gradients in temperature and wind speed and the ground which acts as a nearly rigid reflector for frequencies less than 20 Hz. Two principal propagation channels exist. One between the ground and the stratopause at an altitude of 45 km called the stratospheric duct and a second between the ground and the thermosphere at an altitude of approximately 85 km called the thermospheric duct. These two ducts, illustrated in Figure 2.3 along with the general structure of the atmosphere, act to re-direct infrasonic waves forming 'acoustic channels.' Another more transient source of channeling is the vertical gradient in wind speed associated with the jet stream.[6]

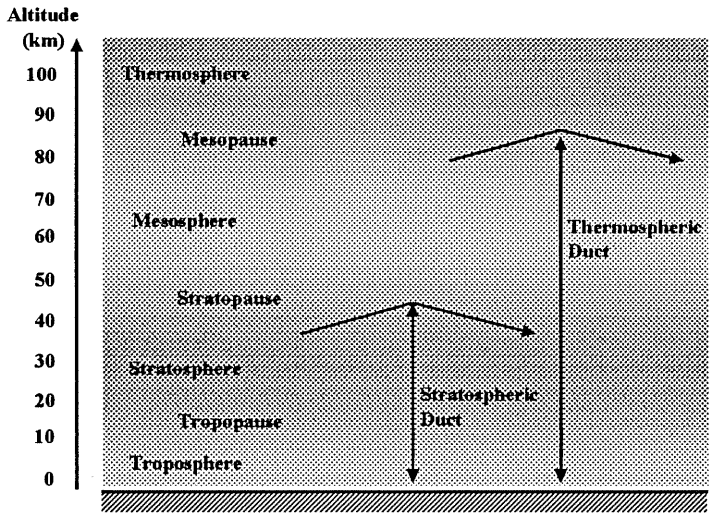

Figure 2.3 Infrasound Propagation Channels

By confining the acoustic waves, channels reduce the attenuation due to geometric spreading, i.e., reducing the parameter g in Equation 2.5, by moving propagation from spherical towards cylindrical as illustrated in Figure 2.4. The change to cylindrical propagation occurs as the spherical acoustic waves are reflected off the ground and refracted by certain layers of the atmosphere such as the stratopause. The horizontal distance from the source at which the propagation will change to cylindrical will be similar to the height of the duct. Considering that the stratospheric duct, the lowest altitude refracting channel, ranges from the ground to approximately 45 km, the change

to cylindrical propagation can be expected to occur approximately 45 km from the source.

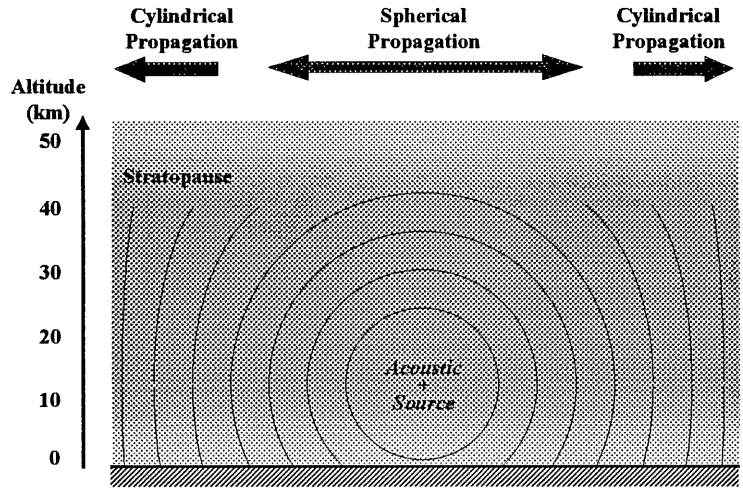

Figure 2.4 Propagation in Atmospheric Channels

2.2 Airborne Particle Characteristics

Understanding airborne particle characteristics is important to this study for two reasons. First, the particle concentration, size and shape distributions are directly linked to backscatter intensity. Second, the size, shape and composition of the particles determine their motion resulting from incident acoustic waves, i.e., the smaller and heavier the particle, the less amplitude for a given acoustic energy density.

Particulate sources include natural combustion events such as forest fires, human activities such as automobile exhaust, windblown dust, emissions of pollen and spores from plants and bursting air bubbles on the surface of the oceans. In addition, events such as volcanic eruptions introduce large quantities of particulates into the atmosphere and can cause significant particle concentration fluctuations. However, these particle concentration fluctuations are mostly confined to the stratosphere and are not significant in the troposphere.[21]

2.2.1 *Particle Concentration, Size Spectra, Shape and Composition*

Atmospheric particles vary in concentration, size distribution and composition as a function of altitude, time and geographic location.[30,34] Particulate concentrations vary from 10^{-6} to 10^{7} particles per cubic centimeter (cm^{-3}). Geographically, typical concentrations range from 1,000 cm^{-3} over oceans, to 10,000 cm^{-3} over land, to 100,000 cm^{-3} in polluted air over cities. On a macro scale, particulates are removed from the atmosphere, primarily through precipitation, at about the same rate they enter.[4]

Particles range in size from about 10^{-4} micrometers to tens of micrometers and are spherical and non-spherical in shape. With respect to particle surface area, size distribution peaks at approximately 0.1 μm diameter with nearly all surface area composed of particles with diameters between 0.01 and 100 μm as illustrated in Figure 2.5. Particle size distribution in marine air, with particles mostly composed of sodium chloride, peaks at slightly larger particle diameters closer to 1.0 μm. The peak distribution shifts toward slightly larger particles at lower altitudes and toward smaller particles at higher altitudes.[12,30,34]

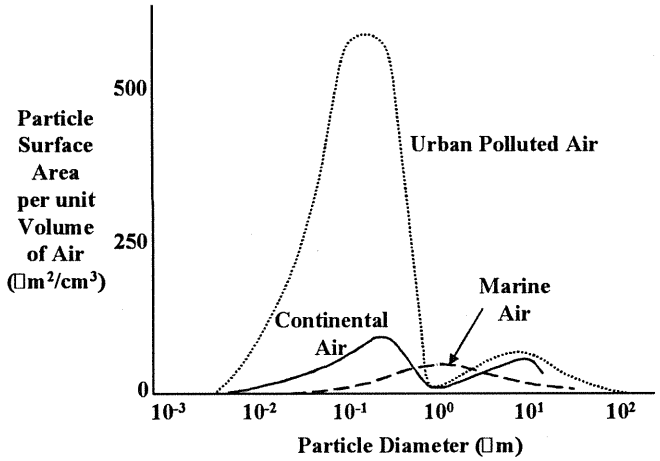

Figure 2.5 Particle Surface Area Distribution[34]

Particle composition consists of large carbon conglomerates (soot), water and soil over land masses and sodium chloride over the oceans. Composition information is necessary to determine particle mass which is a required parameter for the calculation of particle motion in response to acoustic waves.

2.2.2 *Light Backscatter*

The amount of light that is backscattered by particles in the atmosphere is a function of the particle concentration, the particle size and shape and the wavelength of the incident light. Because most the particles are non-spherical and randomly oriented, backscattering deviates from that predicted based on theory. Other substantially more complicated theoretical models have been developed but still show deviation from actual measurements. Therefore, empirical relations were utilized for analyses documented in this report rather than theoretical models.[3]

A significant amount of experimental study has been done over the past decade to determine the empirical backscatter coefficient, β, for various geographical locations, seasonal conditions, laser wavelengths and altitudes throughout the troposphere (nominal altitudes less than 11 km) and stratosphere (altitudes between 11 km and 45 km). The backscatter coefficient units are inverse meter steradians, $m^{-1}sr^{-1}$.

Backscatter coefficient values can vary several orders of magnitude at a fixed location over several hours. This deduction is vividly apparent in the data obtained by the GLOBE missions sponsored by NASA[29] and other studies performed over southeastern Australia and Boulder, Colorado.[12,14,21] These studies covered laser wavelengths from 532 μm to 10.6 μm throughout the troposphere and stratosphere. Backscatter coefficients varied about an order of magnitude across the range of laser wavelengths with higher values for shorter wavelengths. Three characteristic atmospheric particulate layers were observed in the troposphere. The mixed boundary layer ranging from the ground up to approximately 1 km exhibits a backscatter coefficient one or more orders of magnitude greater than in the upper regions of the troposphere. Above the mixed boundary layer, the 'cloud pumped' or transition layer stretches from 1 km to approximately 4 km and the upper-most region of the troposphere from 4 km to 11 km exhibits a low backscatter coefficient. The data also indicate that the backscatter coefficient is slightly higher over land than over the oceans.

Table 2.3 Backscatter Coefficient[12,14,21,29]

Altitude[a]	Atmospheric Region	Backscatter Coefficient ($m^{-1}sr^{-1}$)	
		$\lambda_L = 1.0\ \mu m$[b]	$\lambda_L = 10.6\ \mu m$[b]
0 to 1 km	Mixed Boundary Layer	up to 10^{-5}	up to 10^{-6}
1 to 4 km	Transition Layer	10^{-8} to 10^{-6}	10^{-9} to 10^{-7}
4 to 11 km	Free Troposphere	10^{-9} to 10^{-7}	10^{-10} to 10^{-8}

[a] Altitude ranges for the layers of the atmosphere can vary as much as ± 1 km

[b] λ_L is the laser wavelength

An important physical property of light backscatter incorporated in the empirical backscatter coefficient is the dependency of backscatter efficiency on particle size and the wavelength of the incident light. Particles are most efficient at backscattering light with a wavelength similar to the particle size.

2.3 Doppler Lidar

This section describes the basic principles of Doppler light detection and ranging (lidar) systems that are most relevant to infrasound acoustical detection. This laser application is based on detection the component of motion of particles (atmospheric aerosols) forced by low frequency sound waves. Our assumptions regarding the nature of the acoustic waves and the aerosols are described in the previous two sections.

2.3.1 *Concept Overview*

Doppler lidar is based on measurement of the Doppler frequency shift of the electromagnetic energy reflected by moving objects. The laser's nearly monochromatic emission is reflected by atmospheric aerosols moving relative to the laser source. Ideally,

the portion of the reflected energy received back at the source will also be nearly monochromatic but at a frequency shifted slightly from that of the emitted light.

The laser wavelength is related to the frequency by Equation 2.13 where λ_{Lt} is the transmitted laser wave length in meters, T_t is the period in seconds, f_{Lt} is the frequency in hertz and c is the speed of light in meters per second.

$$\lambda_{Lt} = cT_t = \frac{c}{f_{Lt}} \qquad \text{Eq. 2.13}$$

Let V_D represent the component of relative velocity between the laser and a single reflecting target along the path of the light beam, where V_D is greater than zero when the velocity is away from the laser source. During the time it takes for one cycle of the incident energy to arrive at the target, the target will have moved a distance $V_D T_t$ farther away from the laser when the target is moving away from the observer. Therefore, an observer who is stationary relative to the target will perceive a slightly longer wavelength. The shifted wavelength can be calculated using equation 2.14 where λ_{Lref} is the wavelength of the reflected wave as seen by the observer.

$$\lambda_{Lref} = \lambda_{Lt} + V_D T_t \qquad \text{Eq. 2.14}$$

That portion of the reflected energy that propagates back to the detector co-located with the laser will again be perceived to have a slightly longer wavelength due to the relative motion which is assumed constant over the extremely short path-transit time. The received wavelength, λ_{Lr}, therefore differs by $2V_D T_t$ from the transmitted wavelength, λ_{Lt}, as shown by Equation 2.15.

$$\lambda_{Lr} = \lambda_{Lref} + V_D T_t = \lambda_{Lt} + 2V_D T_t \qquad \text{Eq. 2.15}$$

Combining Equations 2.13 and 2.15 yields Equation 2.16 which expresses the frequency of the received energy as a function of the transmitted frequency and the relative velocity.

$$f_{Lr} = f_{Lt} \frac{1}{\left(1 + \frac{V_D}{c}\right)^2} \approx f_{Lt}\left(1 - 2\frac{V_D}{c}\right) \qquad \text{Eq. 2.16}$$

The approximation in Equation 2.16 is extremely good provided the relative velocity of the target of interest is far from the relativistic speed, c. Thus, the Doppler shift corresponding to the relative velocity V_D is expressed by Equation 2.17 where the negative sign indicates a lower return frequency from receding targets.

$$\Delta f = f_{Lr} - f_{Lt} = -2\frac{V_D}{\lambda_{Lt}} \qquad \text{Eq. 2.17}$$

For the application under consideration in which the 'target' is a suspension of aerosols in a non-static atmosphere, a distribution of relative velocities will actually result. This, in addition to the non-zero bandwidth of the emitted energy by a real laser, results in an extremely complex Doppler signal, which must be processed by the receiver.

2.3.2 *Hardware*

Figure 2.6 contains a high-level block diagram of the essential components of a laser-based system for infrasound detection. These components vary widely among lidar implementations for atmospheric motion detection. Each component is described in the list below.

- *Laser* - This component includes a local oscillator, power supply and energy pumping circuitry, and other components required to deliver a suitably tuned optical signal to the optical system.
- *Optical system* - This component includes focusing and steering systems for both the transmitted and received beams. Its outputs are the optical signals required for heterodyne detection.
- *Detector* - A heterodyne detector converts the optical signals into an RF electrical output signal.
- *Signal Processing* - This component is the most variable among the existing systems. It attempts to detect and, if present, extract the parameters of the atmospheric motion of interest.
- *Telescope* - This component provides the interface between the laser system and the external atmosphere, including both transmission of the high energy output beam and reception of the low energy reflected signal. Most implementations have been monostatic, i.e., a single optical component handles both the transmitted and received energy.
- *Drive* - This is an essential part of all beam scanning systems. As indicated, scanning may be controlled by feedback from the signal processing results.

A concise historical review of the development of lidar technology can be found in the 1996 paper by Huffaker and Hardesty.[13] Detailed block diagrams of several implementations appear in the cited references.[10,21,32] In Table 2.4, the most important performance parameters of several representative pulsed lidar systems are listed. Most of these systems have been implemented and field tested and thus represent potential lidar parameter sets for the acoustic detection application under consideration.

Table 2.4 Representative Pulsed Lidar Systems[13,21,32,33]

Organization/ Application	λ_L	Material	Energy/ pulse	Pulse Width	Pulse Rate
NOAA/Space applications[13]	10 μm	CO_2	1 J	2 - 4 μs	20 Hz
CTI; Wright Lab. & NASA/Wind profiling[13]	1.06 μm	Nd:YAG	200 mJ & 1J		20 Hz
Lockheed-Martin; NASA/Wind hazard detection[32]	2.02 μm	Tm:YAG	1.8 mJ	0.5 μs	200 Hz
CTI; Wright Labs/ Wake vortex detection[13,33]	2.09 μm	Tm,Ho: YAG	20 mJ	0.2 μs	up to 2kHz
Honeywell; Naval Air Warfare Center/On-board air data[21]	2.015 μm	Tm^{3+}: YAG	3 mJ	0.5 μs	> 200 Hz

Material Key: Nd - Neodymium; YAG - yttrium aluminum garnet; Tm - Thulium; Ho -Holmium

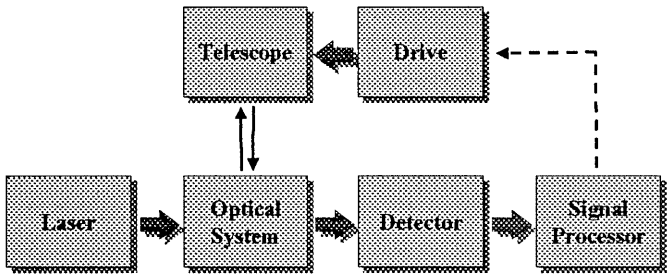

Figure 2.6 Principal Components of a Laser-based Atmospheric Motion Sensor

Applications employing lasers for remote sensing are typically confined to the infrared region of the electromagnetic spectrum due to eye-safety and cost considerations. Infrared wavelengths range from the long wavelength end of the visible spectrum at 0.7 μm through 3,000 μm at the short wavelength end of the microwave spectrum. Wavelength selection for monitoring atmospheric particle motion is influenced by three factors. First, shorter infrared wavelengths approach the visible spectrum and more readily cause eye damage. As a result, eye-safety becomes a primary concern below 2 μm. Second, laser energy backscattered by particles in the atmosphere decreases for

longer infrared wavelengths supporting the selection of a shorter infrared wavelength. And third, velocity accuracy improves with shorter wavelengths. The consensus in recent reports seems to be that pulsed lidar systems based on wavelengths around 2 μm show the most promise for future atmospheric sensing systems, especially for aircraft-based, commercial applications. Advances in materials and optical component construction and assembly makes a coherent, solid-state system at a wavelength of 2 μm feasible.

The lidar systems in Table 2.4 were all designed to detect specific classes of atmospheric motion, e.g., winds, wake vortices or clear air turbulence. Implementing a lidar system to detect turbulence generated acoustic waves will be faced with a new, more challenging set of requirements than those designed to detect atmospheric motion directly.

In the quest for high signal-to-noise ratios, the maximum possible laser power output is desired. Laser power output limitations are governed by technology and eye-safety. Established energy and power limits for lasers are published by the Laser Institute of American as ANSI Z136.1-1993.[36] This text provides a broad range of guidance for safe laser exposure regarding safety. Table 2.5 summarizes laser output limitations showing the significant increase in safe power output for a laser wavelength change from 1.06 to 2.02 μm. The maximum permissible exposure (MPE) values are the energy or power not to be exceeded for continuous wave (CW) lasers. To account for pulsed lasers, the energy or power values in Table 2.5 must be multiplied by $n^{-1/4}$ where n is the number of pulses during the exposure duration. $n^{-1/4}$ ranges from 1.0 to 0.01 for repetitive pulses numbering between 1 and 10^6.

Table 2.5 Continuous Wave Laser Safety Limits[36]

		Maximum Permissible Exposure	
Wavelength (μm)	Exposure Duration, t (s)	Energy (J/cm^2)	Power (W/cm^2)
1.06	10^{-9} to 5.0×10^{-5}	5×10^{-6}	NA
	5×10^{-6} to 10^{-3}	$9.0(t)^{3/4}\times10^{-3}$	NA
	10^{-3} to 3×10^{4}	NA	1.6×10^{-3}
2.02	10^{-9} to 10^{-3}	0.1	NA
	10^{-3} to 10	$0.56(t)^{1/4}$	NA
	10 to 3×10^{4}	NA	0.1
10.6	10^{-9} to 10^{-7}	10^{-2}	NA
	10^{-7} to 10	$0.56(t)^{1/4}$	NA
	10 to 3×10^{4}	NA	0.1

The MPE is the safe radiant energy or power incident on the receiver, e.g., human eye. Therefore, the divergence or convergence of the laser propagation from the transmitter to the receiver must be assessed. Based on the emitted laser power and the optics, the nominal hazard distance (NOHD) can be calculated using Equation 2.18 where r_{NOHD} is the nominal hazard distance in cm, f_0 is the focal length of the lens in cm, b_0 is

the laser beam diameter incident on the lens in cm and Φ is the total or average radiant laser power in watts. Figure 2.7 illustrates the geometry assumed in Equation 2.18. The NOHD is the distance along the axis of the beam beyond which the radiant exposure will not exceed the MPE.

$$r_{NOHD} = \left(\frac{f_0}{b_0}\right)\left(\frac{4\Phi}{\pi(MPE)}\right)^{1/2} \qquad \text{Eq. 2.18}$$

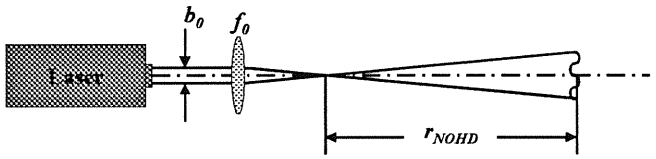

Figure 2.7 Optical Geometry for Calculation of Nominal Hazard Distance

2.3.3 *Signal Processing*

Many of the cited references contain detailed discussions of various signal processing schemes.[5,10,16,17,21,27,28] This section describes the nature of the signal processing problem to support the investigation of limitations that may exist using particular approaches. Equation 2.17 provides a simple proportional relationship between the relative velocity of *any one scatterer* and the received Doppler shift. A pulsed laser transmission with time-gating of the reflected signal to provide information from a specific spatial region will be assumed. The analyzed signal will contain a *distribution* of frequencies, reflecting the range of relative line-of-sight velocities generated by motion of the aerosols within the sampling region.

The relative velocity, V_D, along the line-of-sight from the laser source to any *one* scatterer, i.e., particle, can be expressed as the difference between the velocity of the lidar platform and the particle motion, as in Equation 2.19, where V_{lidar} is the velocity of the lidar system, $V_{particle}$ is the velocity of the particle, V_{wind}, V_{eddy} and $V_{acoustic}$ are the line-of-sight velocity components of the particle due to ambient wind, eddy motion and acoustic waves, respectively.

$$V_D = V_{lidar} - V_{particle} = V_{lidar} - \left(V_{wind} + V_{eddy} + V_{acoustic}\right)_{particle} \qquad 2.19$$

The wind-induced particle velocity will be assumed constant over the interval of time during which data are collected, e.g., no more than a few seconds. The eddy contribution to particle velocity stems from the short-term variability exhibited by small scale turbulence, i.e., eddies, and to random motions of individual aerosols not aligned with the atmosphere's movement. Finally, the acoustic component will induce oscillatory particle motion as the acoustic wave fronts pass through the sample volume.

The peak velocity imparted on the particle by the acoustic waves will be substantially less than the net result of the other terms. Therefore extracting information regarding the acoustic signal must depend on either spatial or temporal scanning by the lidar. While spatial scanning is a conceivable strategy, a temporal approach appears to be more straightforward and will be considered here.

The extensive literature on signal processing is focussed exclusively on single-beam lidars sensing either ambient wind, natural atmospheric turbulence or wave vortices form aircraft which are not directly applicable to the detection of acoustic waves.[5,8,9,27,28] However, some of the references contain valuable material that may prove to be relevant at a later time. The following paragraphs summarize a few of these references.

Discrete Spectral Peak Estimation

Rye and Haresty present an excellent overview of several critical issues in Doppler lidar signal processing, particularly regarding performance bounds implied by signal-to-noise ratios.[27,28] The focus is on spectral accumulation methods for estimating the peak frequency in the Power Spectral Density (PSD) of the Doppler signal.[27] The authors also consider methods based on accumulated autocorrelation estimates, thus avoiding some of the computational costs of the spectral methods.[28] As emphasized earlier, direct relevance of analyses such as these to the acoustic signal detection problem is not obvious due to the need for discriminating between the potentially much larger velocity components associated with atmospheric motion and the much lower velocities resulting from passage of an acoustic wave.

Spectral accumulation refers to averaging a sequence of periodograms of the outputs of an optical heterodyne receiver processing a sequence of pulsed lidar returns. The periodogram is the squared magnitude of the discrete Fourier transform of the sampled signal. The squared magnitude of the periodogram is an estimate of the PSD. Under some circumstances, i.e., moderate sampling rates and adequate computer power, each periodogram can be computed in real-time by state-of-the art digital signal processing hardware. The heterodyne output signal contains frequency components resulting from the *convolution* of the spectrum of the transmitted laser pulse and the spectrum represented by the distribution of velocities in the sensed volume.

Rye and Hardesty showed that under certain assumptions, the Cramer-Rao lower bound on the error variance of an estimate of the spectral peak frequency has the form

shown in Equation 2.20 where n is the number of distinct estimates of the PSD that are accumulated and M is the number of data points used in each of those estimates.

$$\sigma_{CR}^2 = \frac{1}{nM\int(\text{Squared derivative of the logarithm of the PSD})} \qquad \text{Eq. 2.20}$$

The integral in the denominator represents the true signal power and is independent of the sampling and estimation strategy, so it is essentially a constant. Using numerical simulations, the authors showed that this lower bound *can be approached* as n and M get larger. Similar results may hold for an infrasound detection system implementation. That is, by sampling the backscattered laser signal at a very high rate, i.e., high value of n, and accumulating results from enough lidar pulse returns, i.e., high value of M, a future signal processing technique should be able to approach the theoretical limit on accuracy.

Rye and Hardesty also address alternate sets of data processing strategies.[28] Instead of computing the PSD of the sampled data immediately, these approaches calculate an estimate of the autocorrelation function (the correlogram), accumulate those estimates, then calculate the PSD by computing the Fourier transform of the estimate. Because the correlogram requires many fewer multiply and add operations than the PSD computation, this strategy appears to offer advantages in the high data-rate lidar environment. The authors indicate that accuracy similar to that achievable using the periodogram approach can be achieved via these methods.

Edge Technique

The edge technique under development at NASA/Goddard is fundamentally different than the more common heterodyne approach to Doppler-based atmospheric velocity measurement.[10,17] The fundamental idea is illustrated by Figure 2.8. The transmission band of the very-narrow band optical filter is tuned just below the laser transmission frequency, i.e., at a slightly larger wavelength. The mean frequency of Doppler-shifted energy reflected back to the optical system by aerosols also falls along the steep slope of the optical filter characteristic. Therefore, by sensing the difference in the energy transmitted by the filter at the two wavelengths, one can derive the Doppler frequency shift from the known slope of the filter transmission function.

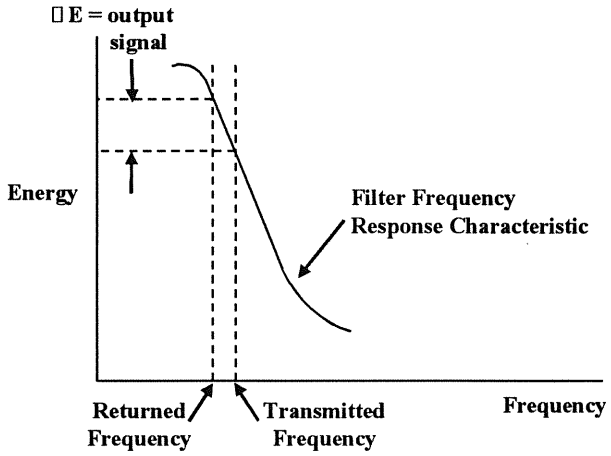

Figure 2.8 Edge Technique for Doppler Shift Estimation[17]

Systems based on the edge technique have been built and tested in both laboratory and real environments. The most recent concept has extended the principle to a double-edge technique to improve overall system performance, but the underlying idea is the same.[16]

3. PARTICLE MOTION CAUSED BY REMOTE ACOUSTIC SOURCE

Particle motion in the atmosphere is driven by air currents and acoustic waves. Air currents can be large-scale currents such as the jet stream, large-scale turbulence such as mountain rotors or small-scale turbulent eddies. All of these air disturbances induce particle motion. However, the interest for this study lies in the detection of particle motion induced by acoustic waves and not by air currents. Static pressure fluctuations related to turbulence exhibit frequencies from 10^{-6} to about 1 Hz and will be treated as a source of noise.[15,25]

Particulates in the atmosphere are acted on by the pressure force associated with the fluctuating pressure gradient inherent to acoustic waves as discussed in Section 2.1.1. As individual wave fronts pass particles suspended in the atmosphere, the increasing and decreasing pressure gradients entrain the particles in the oscillating pressure field. Because the particles are substantially more massive than the air molecules transmitting the acoustic wave, the entrained particles will oscillate with a smaller amplitude than the surrounding air molecules. Also, the larger mass of the particles will cause their oscillatory motion to lag behind that of the air molecules.

The following sections discuss the development of estimates for particle mass and sound pressure level, a model to estimate acoustic induced particle motion and the application of the model to obtain expected particle motion behavior.

3.1 Particle Mass Estimation

Based on the composition and physical characteristics of particles in the atmosphere discussed in Section 2.2.1, the documented particle sizes will be assumed to be spherical diameters. With that assumption, the particle volume can easily be calculated. Particle mass can then be obtained by knowing the density of the particle material. Particle materials include soot, water, soil and sodium chloride.

Soot particles are composed of multiple ring, polynuclear aromatic compounds that are approximately 99% carbon. The particles range from 0.01 μm to 0.2 μm in diameter and contain between 10^5 and 10^6 carbon atoms. Thus, with the atomic weight of carbon at 12.01 grams per mole, i.e., per 6.02×10^{23} carbon atoms, the soot particles have a mass between 2×10^{-18} and 2×10^{-17} grams.[11,23]

Mass estimates for soot particles as well as particles composed of water, soil and sodium chloride are summarized in Table 3.1. The size range assumed in the mass estimates requires further explanation. Although a majority of the particle surface area in the atmosphere is composed of particles with sizes between 0.01 and 100 μm, this size range is not representative of the particles that will most significantly contribute to a light backscatter signal. First, particle surface area in the atmosphere as a function of particle diameter peaks at a particle diameter of approximately 0.1 μm.[34] Second, as discussed in Section 2.2.2, particles with sizes similar to the wavelength of incident light scatter the light most efficiently. Because backscatter intensity is driven both by the particle

concentration and by the backscatter efficiency, the particle sizes with the largest contribution to the backscatter intensity will lie somewhere between 0.1 μm and the laser wavelength. For this study, the laser wavelength are assumed to be between 1.0 and 10.6 μm. Thus, particles with diameters between 0.1 and 10 μm are assumed to contribute to a substantial portion of the laser backscatter. Based on the mass estimates shown in Table 3.1, a particle mass range from 1.0×10^{-17} to 1.5×10^{-9} grams will be assumed in all subsequent analyses.

Table 3.1 Particle Mass Estimates

Composition	Diameter	Density	Mass
Soot	0.1 to 0.2 μm	9.8×10^{4} g/m^3	1.0×10^{-17} to 2.0×10^{-17} g
Water	0.1 to 10 μm	1.0×10^{6} g/m^3	5.2×10^{-16} to 5.2×10^{-10} g
Soil	0.1 to 10 μm	2.8×10^{6} g/m^3	1.5×10^{-15} to 1.5×10^{-9} g
Sodium Chloride	0.1 to 10 μm	2.2×10^{6} g/m^3	1.1×10^{-15} to 1.1×10^{-9} g

3.2 Sound Pressure Level Attenuation

The decay in sound pressure level with increasing distance from the acoustic source can be closely approximated by applying a series of equations. As discussed in Section 2.1.4, the equations combine theoretical and empirical analysis to yield sound pressure level decay with distance as a function of humidity, altitude and acoustic frequency. To facilitate analysis, we implemented an Acoustic Attenuation Model based on the information in Section 2.1.4. Analysis of the two major components contributing to sound pressure level attenuation reveals that geometric spreading accounts for a majority of the total attenuation in contrast to the relatively minimal attenuation due to atmospheric absorption. Because geometric spreading is not a function of atmospheric properties, humidity and altitude would not be expected to have much impact on the total attenuation. This expectation is substantiated through sensitivity analysis results which are plotted in Figures 3.1 and 3.2. Neither humidity nor altitude show significant influence over attenuation for the humidity and altitude ranges of interest. Therefore, analyses do not need to focus on humidity or altitude due to their negligible effect on attenuation in the infrasound regime.

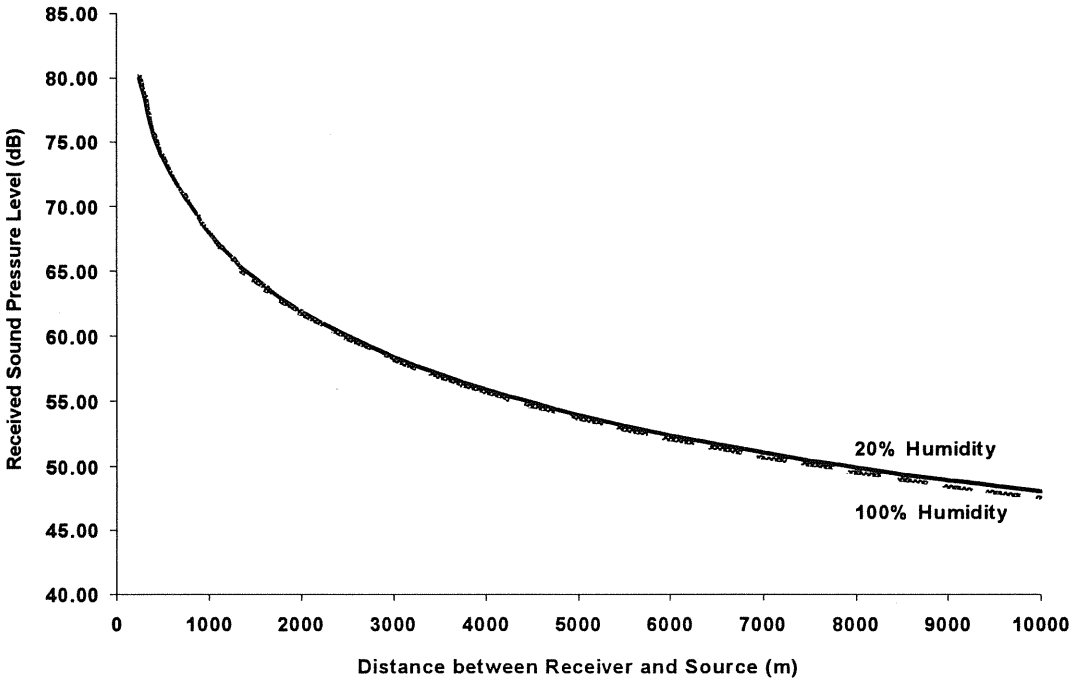

Figure 3.1 Humidity Effect on Attenuation

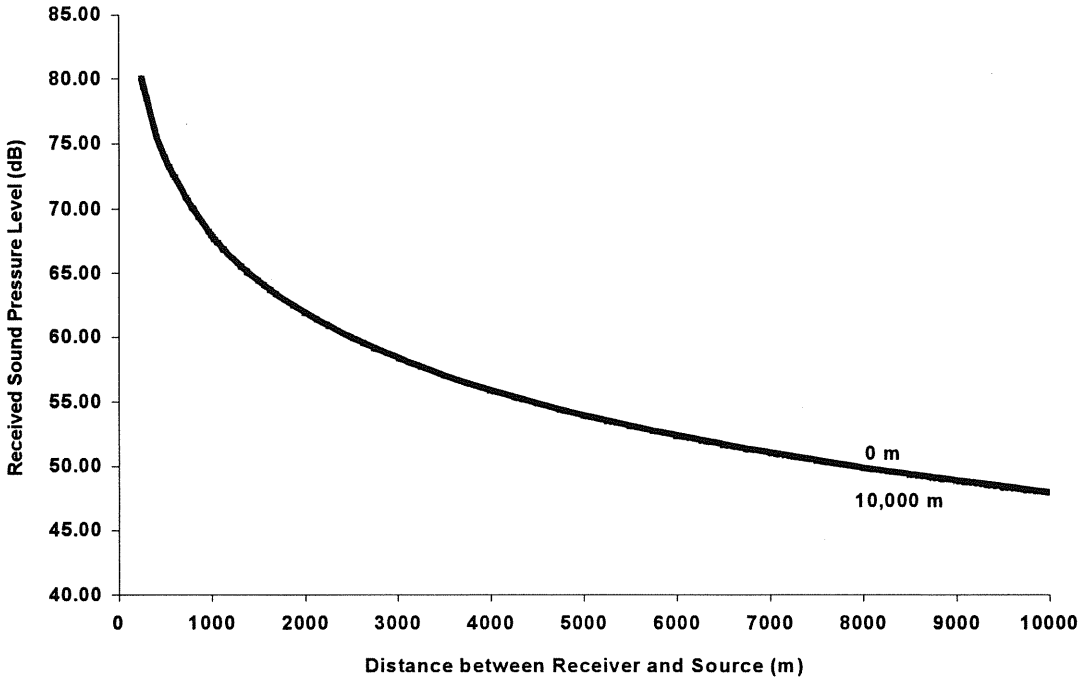

Figure 3.2 Altitude Effect on Attenuation

In addition, we performed sensitivity analysis to investigate attenuation as a function of frequency. Figure 3.3 illustrates the significant reduction in attenuation for decreasing frequencies from 10,000 Hz to 0.01 Hz, i.e., drop through the audible into infrasound. The substantial increase in acoustic attenuation for frequencies above the infrasound region, i.e., greater than 20 Hz, are prohibitive for detection of acoustic waves at ranges greater than 10 km. Within the infrasound region of the acoustic spectrum, significantly less reduction in attenuation with decreasing frequency is observed as shown by comparison of the attenuation curves for frequencies of 10 Hz and 0.01 Hz.

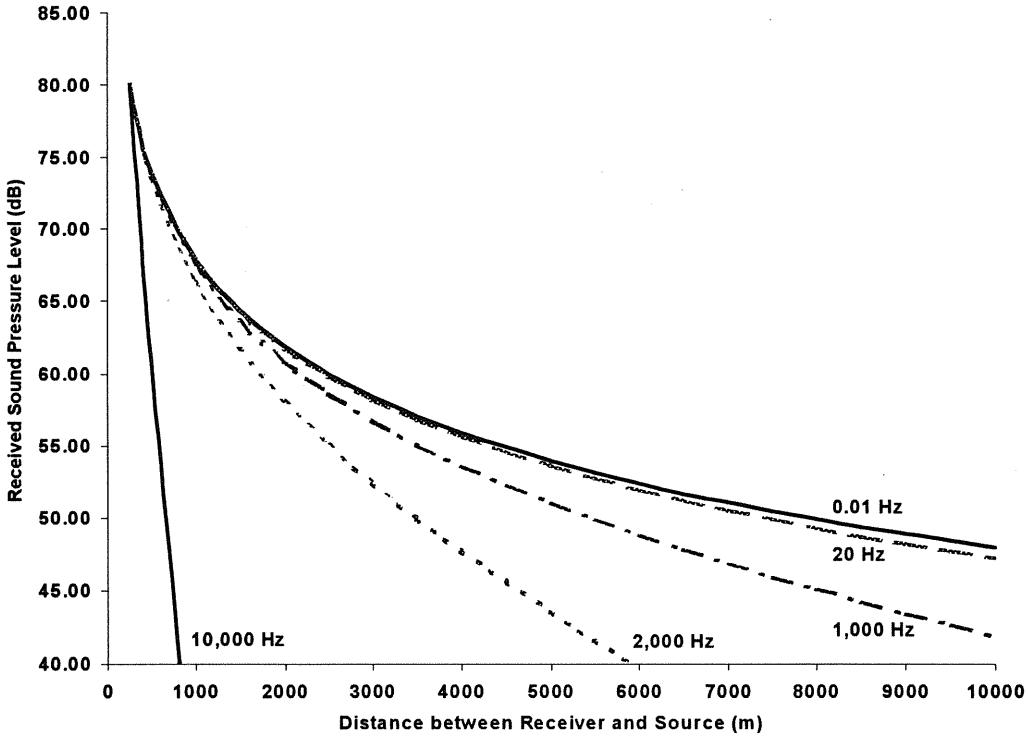

Figure 3.3 Acoustic Frequency Effect on Attenuation

We applied the Acoustic Attenuation Model for source distances of 1, 10 and 20 km. The analysis considered ranges of sound pressure level, frequency and altitude based on the available information on turbulence-generated acoustic waves in Table 2.1. Acoustic waves were conservatively assumed to propagate spherically. The reported sound pressure levels were assumed to be at a distance 25 km from the source for mountain waves and CAT and at a distance of 300 km for storms based on the measurement descriptions. Applying the model with the stated assumptions, the expected ranges of sound pressure level for three given distances from turbulence acoustic sources were calculated and are shown in Table 3.2.

Table 3.2 Sound Pressure Level Attenuation Analysis

Source	Frequency Range	Sound Pressure Level		
		1 km[a]	10 km[a]	20 km[a]
Mountain Waves	0.02 – 0.1 Hz	102 – 132 dB	82 – 112 dB	76 – 106 dB
Severe Storms	0.02 – 10 Hz	118 – 149 dB	98 – 129 dB	92 – 122 dB
CAT	1 – 16 Hz	107 – 115 dB	87 – 95 dB	81 – 88 dB

[a] Distance from acoustic source, i.e., turbulence

3.3 Particle Motion

A particle motion model was developed based on several simplifying assumptions. Due to the *random shape and orientation* of atmospheric aerosols, the particles were assumed to be disc-like in shape with radius and height r as illustrated in Figure 3.4. This assumption will cause the model to predict slightly higher entrainment than would exist for spherically shaped particles. The acoustic wave was assumed to propagate in a compressible and isentropic atmosphere where the medium behaves as an ideal gas. In Figure 3.4, P_{S1} is the static pressure on the upstream side of the particle, P_{S2} is the static pressure on the downstream side of the particle, ρ is the air density, V is the relative velocity between the air molecules and the particle, $V_{particle}$ is the velocity of the particle, A is the area of the particle perpendicular to the direction of the propagating acoustic waves, m is the mass of the particle and a is the acceleration of the particle. As acoustic wave fronts pass the particle, the particle experiences forces from the static pressure differential across the particle, $(P_{S1}A-P_{S2}A)$, the dynamic pressure of impinging air molecules, $2\rho V|V|A$, and acceleration, ma.

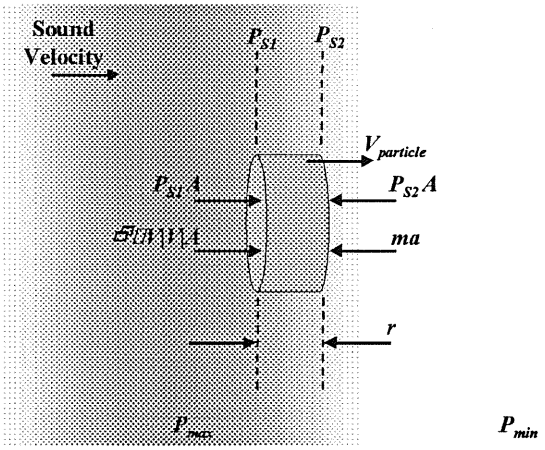

Figure 3.4 Particle Force Diagram

Balancing the forces on the particle yields Equation 3.1. Solving for the particle acceleration gives Equation 3.2 where ΔP_S is the static pressure differential across the particle.

$$P_{S1}A+\frac{1}{2}\rho V|V|A=P_{S2}A+ma \qquad \text{Eq. 3.1}$$

$$a=\frac{\left(P_{S1}+\frac{1}{2}\rho V|V|-P_{S2}\right)A}{m}=\frac{\left(\Delta P_S+\frac{1}{2}\rho V|V|\right)A}{m} \qquad \text{Eq. 3.2}$$

Now, the oscillating variables in Equation 3.2, namely the static pressure differential, the air density and the relative velocity between the air molecules and the particle, need to be solved for in terms of maximum acoustic pressure, acoustic frequency and atmospheric conditions. The governing equations of motion satisfying continuity, momentum and energy conservation for an acoustic wave can be written as Equations 3.3 based on the previously stated assumptions. In Equations 3.3, p is pressure, x is position, t is time, c_p is specific heat at constant pressure, c_v is specific heat at constant volume, u is air molecule velocity, ρ is density and the zero subscripts denote stagnation values. (Ref. 20)

$$\frac{\partial p}{\partial t}+\frac{c_p}{c_v}p_0\frac{\partial u}{\partial x}=0$$

$$\frac{\partial \rho}{\partial t}+\rho_0\frac{\partial u}{\partial x}=0 \qquad \text{Eqs. 3.3}$$

$$\frac{\partial^2 u}{\partial t^2}-\frac{c_p}{c_v}\frac{p_0}{\rho_0}\frac{\partial^2 u}{\partial x^2}=0$$

A solution to this set of equations can be expressed in the form shown in Equations 3.4, where P_{max} is the maximum acoustic pressure, $v_s=\sqrt{\gamma RT}$ is the sound velocity, f is the acoustic frequency.

$$u(x,t)=\frac{P_{\max}}{v_s\rho_0}\cos\left(\frac{2\pi f}{v_s}(x-v_s t)\right)$$

$$p(x,t)=P_{\max}\cos\left(\frac{2\pi f}{v_s}(x-v_s t)\right) \qquad \text{Eqs. 3.4}$$

$$\rho(x,t)=\frac{P_{\max}}{RT}\cos\left(\frac{2\pi f}{v_s}(x-v_s t)\right)$$

The air molecule displacement, s, is obtained by integrating the solution for velocity, $u(x,t)$, with respect to time and is written as Equation 3.5.

$$s = -\frac{P_{\max}}{v_s \rho_0 (2\pi) f} \sin\left(\frac{2\pi f}{v_s}(x - v_s t)\right) \qquad \text{Eq. 3.5}$$

The static pressure differential across the particle can be expressed as Equation 3.6 where $\frac{2\pi f}{v_s} r$ is the phase shift corresponding to the particle radius, r, which is usually extremely small for the acoustic frequencies of interest.

$$\Delta P_S = P_{\max}\left[\cos\left(\frac{2\pi f}{v_s}(x - r - v_s t)\right) - \cos\left(\frac{2\pi f}{v_s}(x + r - v_s t)\right)\right] \qquad \text{Eq. 3.6}$$

Finally, the relative velocity between the air molecules and the particle can be calculated by subtracting the particle velocity from the air molecule velocity as shown by Equation 3.6.

$$V(x,t) = u(x,t) - V_{particle} = \frac{P_{\max}}{v_s \rho_0} \cos\left(\frac{2\pi f}{v_s}(x - v_s t)\right) - V_{particle} \qquad \text{Eq. 3.7}$$

The particle motion model based on Equations 3.1 through 3.7 was coded in Matlab and applied to determine particle velocity as a function of sound pressure level, acoustic frequency, altitude and particle size and mass. Particle cross-sectional area divided by particle mass is a convenient parameter to express particle entrainment characteristics. The larger the value of this entrainment parameter, the easier the particle will be entrained. Based on the estimates in Section 3.1, the entrainment parameter can be expected to range from a minimum of 1.5×10^{1} to a maximum of 5.2×10^{4} m^2/kg. The modeling results for the considered turbulence events over the expected range of the entrainment parameter, Table 3.3, show a range of velocity fluctuation amplitudes from approximately 10^{-6} to 0.3 meters per second. The amplitude of the particle velocity fluctuation increases with increasing sound pressure level and altitude and decreases with increasing acoustic frequency. As expected, the amplitude of the particle velocity increases towards the air molecule velocity as the entrainment parameter increases.

Taking a closer look at particle entrainment in a fluctuating field of air molecules, the air molecule and particle velocities are plotted in Figures 3.5 and 3.6 for area to mass ratios of 15,000 and 150 m^2/kg, respectively. The substantially higher area to mass ratio in Figure 3.5 results in the particle being almost completely entrained with the air molecules, i.e., the particle velocity lags in phase and magnitude only a small amount compared with that of the air molecules. In contrast, the low area to mass ratio in Figure 3.6 results in a very small entrainment of the particle with the air molecules, i.e., the particle lags in phase and magnitude significantly from that of the air molecules.

Table 3.3 Particle Velocity Fluctuation Amplitude

	Particle	Acoustic		Fluctuation Amplitude	
Altitude (km)	Area/Mass (m^2/kg)	SPL (dB)	Freq (Hz)	Air (m/s)	Particle (m/s)
Mountain Waves					
0	52	76	0.1	4.3×10^{-4}	1.0×10^{-5}
11	52	76	0.1	1.7×10^{-3}	3.7×10^{-5}
0	16,000	106	0.02	1.4×10^{-2}	1.4×10^{-2}
11	16,000	106	0.02	5.2×10^{-2}	5.2×10^{-2}
Severe Storms					
0	52	92	10	2.7×10^{-3}	5.3×10^{-6}
11	52	92	10	1.0×10^{-2}	2.1×10^{-5}
0	16,000	122	0.02	8.5×10^{-2}	8.5×10^{-2}
11	16,000	122	0.02	3.3×10^{-1}	3.3×10^{-1}
Clear Air Turbulence					
0	52	81	16	7.6×10^{-4}	2.7×10^{-7}
11	52	81	16	1.7×10^{-3}	1.2×10^{-6}
0	16,000	88	1	2.9×10^{-3}	1.6×10^{-3}
11	16,000	88	1	6.6×10^{-3}	6.2×10^{-3}

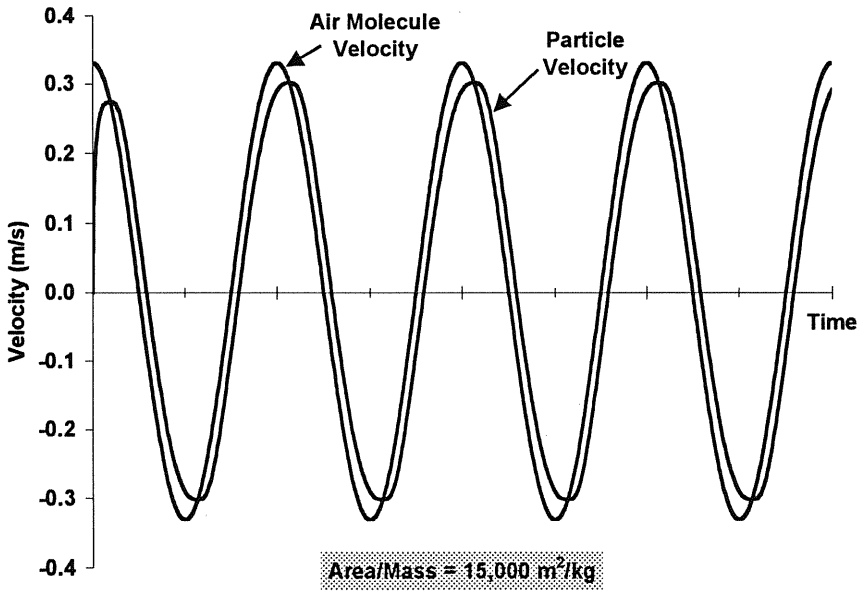

Figure 3.5 Low Frequency, High Area/Mass Velocity Profile

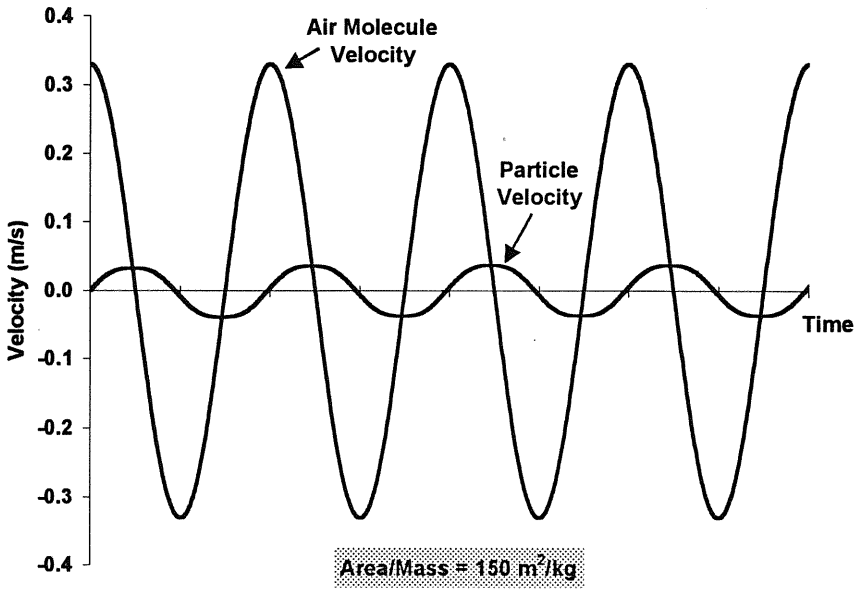

Figure 3.6 High Frequency, Low Area/Mass Velocity Profile

Turbulent motion of the atmosphere will also entrain and induce oscillatory motion on particles in the atmosphere. When turbulent motion exists in the sampling volume of the detection system, the backscatter signal will reflect wavelength shifts from the particle motion induced by acoustic waves as well as by turbulent motion. As observed by instrumented aircraft, turbulent motion of the atmosphere exhibits velocity fluctuations with amplitudes ranging from 1 to 7 m/s. These fluctuations have frequencies as high as 20 Hz but a majority of their spectral power is at frequencies less than 0.1 Hz. Although the majority of the spectral power is not focused in the frequency region for acoustic detection, the upper frequency range of these fluctuations does enter the acoustic frequency range of interest. Turbulent motion must therefore be considered as a source of noise or interference.[15,24,25]

4. PARTICLE MOTION DETECTION USING A SINGLE LASER BEAM

This chapter discusses various aspects of applying a lidar-based system to detect turbulence generated acoustic waves based on the physics and technology review in Chapter 2 and the particle motion analysis in Chapter 3. As the fundamentals of the application are discussed, associated technical challenges are identified. The following discussion does not attempt to focus on any defined lidar-based system design but instead approaches the application from a fundamental concept level. Figure 4.1 illustrates the assumed configuration with a focused sampling volume at a distance f_0 from the lidar unit. The sampling volume extends to the half-power distance, dR, on both sides of the focal distance. The parameter D represents the distance from the center of the sampling volume to the acoustic source and is assumed to be much larger than f_0. The sampling volume shape illustrated in Figure 4.1 is typical for continuous wave lidar systems although this discussion will also consider pulsed systems. A laser wavelength of 2.0 μm is assumed based on consideration of backscatter coefficient, eye safety power limit, atmospheric extinction and velocity measurement accuracy.[18]

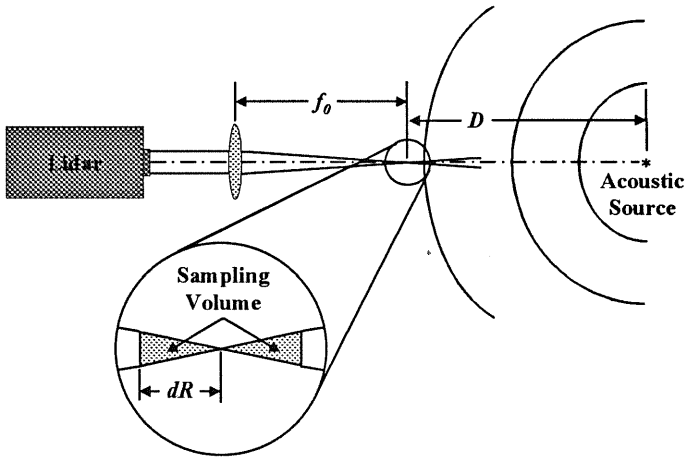

Figure 4.1 Assumed Laser Detection System Configuration

4.1 Ground Level

Ground-based applications include aircraft wake vortex detection in approach and departure paths at airports and turbulence detection at high-risk enroute locations such as mountain rotor detection near the continental divide in Colorado. Both of these applications provide a stationary, ground-level instrument platform. The sampling volume projected from this platform will lie in the lowest tier of the troposphere where particle densities, and hence backscatter coefficient values, are at a maximum.

A lidar system remotely senses the velocity of atmospheric particles by monitoring the wavelength of laser light backscattered from the particles. Assuming that the particles are completely entrained with the air molecule motion, the velocity of the air molecules will be identical to that measured for the particles, i.e., air molecule velocity is

sensed indirectly through the particles. The application of lidar to detect acoustic waves in which air and particle motion is oscillatory rather than measuring relatively steady-state velocities, such as wind or even wake vortices, introduces additional complexities.

Contrasting the two applications, the radical difference becomes apparent. Figure 4.2 illustrates a simplified received lidar signal varying around a steady-state velocity with a noise floor. In the common, steady-state application, the component of interest is the steady-state velocity. The backscattered laser energy is analyzed over an interval of time for several sample and analysis cycles. The received signal will slightly fluctuate over time due to the presence of acoustic waves and small-scale turbulence present in the sampling volume. For this application the acoustic waves and small scale turbulence are a source of noise. By processing signals collected over time, the fluctuating component can be effectively averaged out, improving signal-to-noise ratio (SNR) and providing a more accurate velocity measurement.

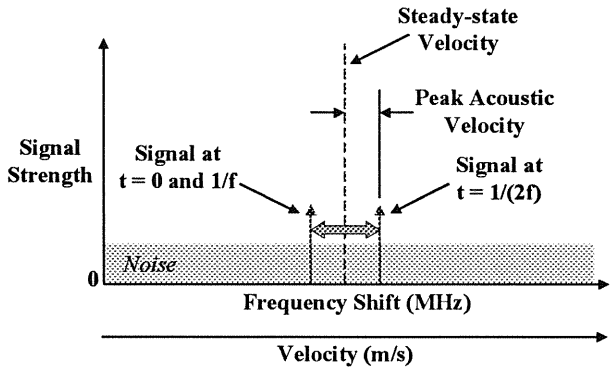

Figure 4.2 Lidar Signal

In contrast to the steady-state application, single-laser acoustic detection is a non-steady-state lidar application in which the velocity component of interest is sinusoidally oscillating with an amplitude proportional to the peak acoustic velocity. The primary interest lies in resolving the acoustic power spectrum across a range of frequencies, e.g., 0.01 to 10 Hz. The lidar-based detection system would therefore have to collect samples at or above 20 Hz, i.e., the Nyquist frequency for the highest frequency of interest. Referring to Table 2.4, lidar systems currently exist with pulse rates as fast as 2,000 Hz. Provided that signal processing can keep up with signal collection at the pulse rate, existing lidar systems provide sufficient sampling rates to resolve the power spectrum over the range of frequencies.

The same fixed volume in space must be repeatedly sampled in order to collect a sufficient number of signals to produce each acoustic power spectrum. For ground-based applications, the lidar platform is stationary and repeated sampling is not an issue provided that minimal wind is present in the sampling volume. However, improving

SNR would require averaging multiple signals at the same position along the acoustic wave, i.e., the sampling volume would have to track with the acoustic waves moving at the speed of sound. Thus, improving SNR by averaging multiple signals is substantially complicated by the oscillatory nature of the signal component of interest when compared with the more common lidar application to detect relatively steady-state velocity.

In addition, the received lidar signal is composed of backscattered laser light from numerous particles with a range of area-to-mass ratios. Therefore, the signal corresponding to the velocity magnitude will be observed not as the singular velocity illustrated in Figure 4.2, but rather as a blurred continuum of velocities oscillating about some steady-state velocity. The signal blurring will significantly challenge and complicate the signal processing necessary to transform the received signal to the desired acoustic power spectrum. A minimum peak acoustic velocity for which an acoustic power spectrum can be obtained will exist based on the signal blurring and signal processing capabilities.

All contributions to particle velocity within the sampling volume will be reflected in the obtained acoustic power spectrum. The particle velocity relative to the lidar system can be obtained by expanding Equation 2.19 to yield Equation 4.1 assuming that the lidar is a stationary, ground-based system. Particle motion induced by wind is represented by the first term in the equation and will not contribute significantly to the acoustic power spectrum due to it's relatively steady-state nature. However, the second term in the equation representing eddy motion, e.g., small-scale turbulence, present in the sampling volume will induce particle motion with a characteristic frequency related to the length scale and velocity of the eddies and will contribute to the obtained acoustic power spectrum. The third term represents the oscillatory particle motion induced by acoustic waves present in the sampling volume including the source of interest, i.e., turbulence-generated acoustic waves. As discussed in Section 2.1.2, numerous acoustic waves not generated by turbulence will also potentially induce oscillatory particle motion. Thus, the obtained acoustic power spectrum will not be exclusive to turbulence-generated acoustic waves and will therefore necessitate additional processing to filter out unwanted acoustic components, e.g., eddy motion and acoustic waves not generated by turbulence.

$$V_D(t) = -V_{wind} - V_{eddy}\cos(2\pi f_{eddy}t + \varphi_{eddy}) - V_{acoustic}\cos(2\pi ft) \qquad \text{Eq. 4.1}$$

Particle motion analysis in Chapter 3 showed that maximum peak velocities of particles entrained by turbulence-generated acoustic waves are on the order of 0.05, 0.3 and 0.006 m/s for mountain waves, severe storms and clear air turbulence, respectively. These values result from the maximum area-to-mass ratio particles driven by acoustic waves with frequencies of 0.02 Hz for mountain waves and severe storms and 1 Hz for clear air turbulence as shown in Table 3.3. Particle entrainment and hence peak acoustic velocity drop off rapidly for frequencies above 1 Hz and/or for particles characterized by smaller area-to-mass ratios. However, as shown in Figures 3.5 and 3.6, the less entrained particles still oscillate at the acoustic frequency but with lower peak velocities. The frequency of the Doppler signal is directly proportional to the particle velocity. This

equation also represents the form of the spectrum derived from a pulse reflected by the particles at time *t*.

For a 2 μm laser wavelength, Equation 2.17 shows that a relative velocity of 1 m/s yields a 1 MHz Doppler shift. Thus, the spectrum of the actual signal received by the detector will be the convolution of Equation 4.1 with the spectrum of the transmitted laser pulse in units of m/s or MHz. Since the frequency of the laser pulse is not a monochromatic source and contains a continuum of frequencies surrounding the lidar central frequency, the laser output itself is not ideal since it contains energy throughout a small finite bandwidth. However, this effect is much smaller than the spreading due to pulse switching. The amount of spreading can be controlled to some extent through careful design of the switching mechanism.

The bandwidth of a pulsed signal is proportional to the reciprocal of the pulse width. Existing lidar systems are capable of producing pulse widths of approximately 0.5 μs yielding a 2 MHz bandwidth. Following heterodyning, the acoustic term in the Doppler signal will oscillate between ±0.3 MHz for the maximum possible peak acoustic velocity of 0.3 m/s. The ±0.3 MHz is well inside the 2 MHz bandwidth associated with a 0.5 μs pulse making signal processing extremely difficult.

The lidar system must sense a spatial region substantially shorter than the minimum acoustic wavelength as illustrated in Figure 4.3. The simple distance versus time diagram shown in Figure 4.4 illustrates the relationship between the pulse width, gating time and the sampling distance. The lines marked *leading* and *trailing* indicate positions of the leading and trailing edges of the transmitted pulse as functions of time and pulse width, T_P. The positions of the leading and trailing edges of the reflected pulse with slope equal to the speed of light, $-c$, are to the right in the diagram. The sampling distance ΔD is that from which energy is received during the gate interval T_0 to (T_0+T_G). As the length of the gate, T_G, decreases to zero, ΔD decreases to its minimum possible value of 75 m, calculated using Equation 4.2 for a 0.5 μs pulse width.

$$\Delta D_{\min} = \frac{1}{2} c T_P \qquad \text{Eq. 4.2}$$

To obtain a sensed volume length that is one eighth the minimum acoustic wavelength of 29.5 m, Equation 4.2 requires a pulse width less than 25 ns which is far faster than the state-of-the-art systems summarized in Table 2.4. Furthermore, since the amount of energy in the received signal is proportional to the gate length, SNR requirements typically lead to gate lengths on the order of the pulse width, and therefore, sensed volumes on the order of $2\Delta D_{min}$ or 150 m. Thus, existing lidar systems employed for atmospheric velocity measurement do not achieve pulse widths short enough to yield sufficient spatial resolution to obtain useful velocity data. Reducing the pulse width to improve the spatial resolution will only increase the bandwidth, further obscuring the oscillating signal created by the acoustic wave.

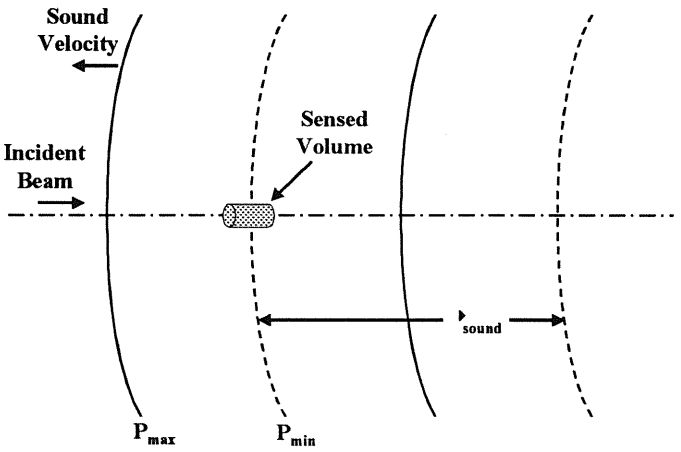

Figure 4.3 Lidar Sensing Volume

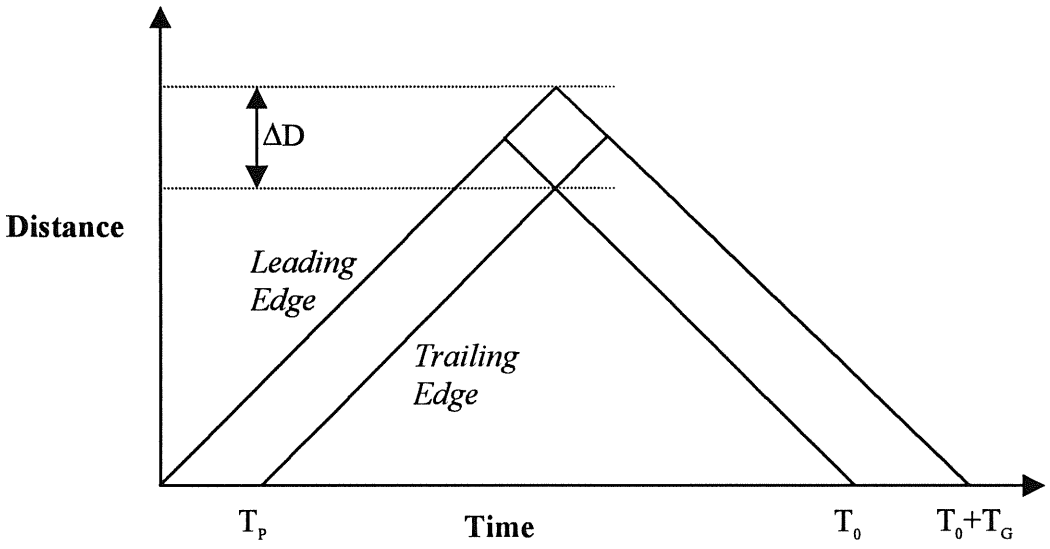

Figure 4.4 Laser Pulse Distance vs. Time Diagram

4.2 Aircraft Cruise

Lidar application to detect turbulence from onboard an aircraft introduces additional complications to those for ground-level application. Aircraft typically cruise at altitudes around 11 km and at speeds of approximately Mach 0.9. The speed of sound at 11 km is approximately 295 m/s corresponding to a aircraft cruise speed of 265 m/s. The motion of the lidar platform, V_{lidar} in Equation 4.3, introduces an additional Doppler frequency shift component due to the aircraft cruise speed. For a 2 μm laser, the observed backscatter signal from particles in a motionless atmosphere will be shifted by 0.265 GHz. Another complication is the significantly lower particle density at cruise altitude

resulting in a two to three order of magnitude drop in backscatter coefficient from ground level to 11 km. This will result in a much decreased SNR compared with that at ground-level.

$$V_D(t) = V_{lidar} - V_{wind} - V_{eddy}\cos(2\pi f_{eddy}t + \varphi_{eddy}) - V_{acoustic}\cos(2\pi ft) \qquad \text{Eq. 4.3}$$

Collecting a sufficient number of samples from the same fixed volume in space to produce each acoustic power spectrum is substantially complicated by aircraft motion. For a 20 Hz sampling frequency, the time between samples is about 50 ms. Each sample is the result of processing data from several pulses and gate intervals to provide adequate SNR. At the 265 m/s closing velocity, the laser propagation path length will shorten by 13.25 m between samples, necessitating continuous adjustment of the time gate as additional measurements are collected. To obtain ten samples, therefore, would require acquisition of the first sample from a volume approximately 150 m in front of the aircraft and the last sample from a volume approximately 20 m in front of the aircraft. While this is feasible with current laser systems, it introduces a minimum pulse power limit to cope with backscatter dispersion and attenuation and maintain an acceptable SNR.

5. CONCLUDING REMARKS

The research and analysis documented in this report provides a high-level look into the physics, technology and application issues regarding single laser detection of particle motion induced by turbulence-generated infrasound. The following list summarizes the identified challenges confronting the development and application of such a detection system.

- The acquisition and averaging of multiple signals typically employed by Doppler lidar systems to improve signal-to-noise ratio is substantially complicated by the oscillatory nature of the acoustic signal component of interest.

- Signal quality and signal processing capabilities limit the minimum sound pressure level for which an acoustic power spectrum can be obtained. Thus, the established threshold for the weakest turbulence event which the system will be expected to detect will impart stringent requirements on hardware and signal processing software.

- Existing Doppler lidars do not produce pulse widths short enough to yield sufficient spatial resolution to obtain velocity data containing the long wavelength acoustic components of interest.

- The acoustic Doppler signal can be expected, at a maximum, to oscillate between ±0.3 MHz within a 2 MHz bandwidth for a 0.5 μs pulse width. Reducing the pulse width to improve the spatial resolution will increase the band width, further obscuring the oscillating signal created by the acoustic wave.

- The obtained acoustic power spectrum will not be exclusive to turbulence-generated acoustic waves and will therefore necessitate additional processing to filter out unwanted acoustic components, e.g., eddy motion and acoustic waves not generated by turbulence. This additional processing will be computationally intensive introducing a substantial processing demand on the system.

- The two to three order-of-magnitude drop in backscatter coefficient at aircraft cruise altitude compared with that at ground-level will significantly reduce the signal-to-noise ratio making detection at cruise altitude difficult.

- The substantial increase in relative velocity between the lidar system platform and the propagating acoustic waves at aircraft cruise velocity complicates the acquisition of multiple signals from the same spatial region necessary to obtain acoustic power spectrum data.

Numerous challenges stand before the application of a single beam Doppler lidar system for the detection of turbulence generated acoustic waves. However, many of these challenges may be overcome through the use of a multiple laser beam system and the application of emerging lidar and signal processing technologies.

References

1. Bedard, A.J. "Atmospheric Turbulence Aloft: A Review of Possible Methods for Detection, Warning and Validation of Prediction Models," American Institute of Aeronautics and Astronautics, 31st Aerospace Sciences Meeting & Exhibit, Paper No. 93-0847, January 1993.
2. Bedard, A.J. "Infrasound Originating Near Mountainous Regions in Colorado," Journal of Applied Meteorology, Vol. 17, pp. 1014 – 1022, 1978.
3. Bohren, C.F., Nevitt, T.J. and Singham, S.B. "Infrared Backscattering," National Aeronautics and Space Administration, NTIS Publication N90-12083/3, 1989.
4. Cliff, W.C. and Huffaker, R.M. *Application of a Single Laser Doppler System to the Measurement of Atmospheric Winds*, NASA Technical Memorandum TM X-64891, October 1974.
5. Constant, G., Foord, R., Forrester, P.A. and Vaughan, J. M. "Coherent laser radar and the problem of aircraft wake vortices," J. of Modern Optics, Vol. 41, No. 11, pp. 2153-2173, 1994.
6. Crocker, M.J. Handbook of Acoustics, John Wiley & Sons, Inc., 1998.
7. Dutton, J.A. The Ceaseless Wind, McGraw-Hill, Inc., pp. 464-465, 1976.
8. Frehlich, R.G. and Yadlowsky, M. J. "Performance of mean-frequency estimators for Doppler radar and lidar," J. of Atmospheric and Oceanic Technology, Vol. 11, pp. 1217-1230, October 1994.
9. Frehlich, R.G., "Performance of a 2-μm coherent Doppler lidar for wind measurements," J. of Atmospheric and Oceanic Technology, Vol. 11, pp. 1517-1528, December 1994.
10. Gentry, B.M. and Korb, C.L. "Edge technique for high-accuracy Doppler velocimetry," Applied Optics, Vol. 33, No. 24, pp. 5770-5777, 20 August 1994.
11. Glassman, I. Combustion, 2nd Edition, pp. 361 – 362, Academic Press, Inc., 1987.
12. Gras, J.L. et. al. "Southern Hemisphere Tropospheric Aerosol Backscatter Measurements – Implications for a Laser Wind System," Journal of Geophysical Research, Vol. 96, No. D3, pp. 5357 – 5367, March 1991.
13. Huffaker, R.M. and Hardesty, R.M. "Remote sensing of atmospheric wind velocities using solid-state and CO_2 coherent laser systems," Proceedings of the IEEE, Vol. 84, No. 2, pp. 181-204, February 1996.
14. Kent, G.S. and Yue, G.K. "The Modeling of CO_2 Lidar Backscatter from Stratospheric Aerosols," Journal of Geophysical Research, Vol. 96, No. D3, pp. 5279 – 5292, March 1991.
15. Khalaf, C.S. and Stoughton, J.W. "Design of Infrasound-Detection System via Adaptive LMSTDE Algorithm," National Aeronautics and Space Administration, NAS1-17099 Final Report, 1984.

16. Korb, C.L., Gentry, B.M., Li, S.X. and Flesia, C. "Theory of the double-edge technique for Doppler lidar wind measurement," Applied Optics, Vol. 37, No. 15, pp. 3097-3104, 20 May 1998.

17. Korb, C.L., Gentry, B.M. and Weng, C.Y. "Edge technique: theory and application to the lidar measurement of atmospheric wind," Applied Optics, Vol. 31, No. 21, pp. 4202-4213, 20 July 1992.

18. Lawrence, T.R. "The Effects of Wavelength on Coherent Doppler Lidar Performance," Proceedings of the NASA Symposium on Global Wind Measurements, pp. 183 – 187, A. Deepak Publishing, Science and Technology Corporation, Hampton, VA, 1985.

19. Masdea, A., Michelangeli, G.B. and Cosentino, A. "Receiver and transmitter design criteria in coherent Doppler wind lidar," in *Lidar Techniques for Remote Sensing*, SPIE Vol. 2310, pp. 174-184, 1994.

20. Menzies, R.T. and Tratt, D.M. "Airborne CO_2 lidar for measurements of atmospheric aerosol and cloud backscatter," *Applied Optics*, Vol. 33, No. 24, pp. 5698-5711., 20 August 1994

21. Mocker, H.W. and Wagener, T.J. "Laser Doppler Optical Air-data System: Feasibility Demonstration and Systems Specification," Journal of Applied Optics, Vol. 33, No. 27, September 1994.

22. Moore, C.S., White, S.W., Karl, R.R. and Newman, B.E. "Directional wind-measurement derived from elastic backscatter lidar data in real-time," SPIE Vol. 2748, pp. 283-288, 1996.

23. Palmer, H.B. and Cullis, H.F. "The Chemistry and Physics of Carbon," Vol. 1, p. 265, Marcel Dekker, New York, 1965.

24. Posmentier, E.S. "1- to 16Hz Infrasound Associated with Clear Air Turbulence Predictors," Journal of Geophysical Research, Vol. 79, No. 12, April 1974.

25. Rhyne, H.R., Murrow, H.N. and Sidewell, K. "Atmospheric Turbulence Power Spectral Measurements to Long Wavelengths for Several Meteorological Conditions."

26. Richmond, R., Henderson, S.W. and Hale, C.P. "Atmospheric effects on laser propagation comparisons at 2 and 10 microns," SPIE Vol. 1633, *Laser Radar VII*, pp. 74-85, 1992.

27. Rye, B.J. and Hardesty, R.M. "Discrete spectral peak estimation in incoherent backscatter heterodyne lidar. I: Spectral accumulation and the Cramer-Rao lower bound,:" IEEE Transactions of Geoscience and Remote Sensing, Vol. 31, No. 1, pp. 16-27, January, 1993.

28. Rye, B.J. and Hardesty, R.M. "Discrete spectral peak estimation in incoherent backscatter heterodyne lidar. II: Correlogram accumulation," IEEE Transactions of Geoscience and Remote Sensing, Vol. 31, No. 1, pp. 28-35, January, 1993.

29. Spinhirne, J.D., Chudamani, S. and Cavanaugh, J.F. "Visible and Near IR Lidar Backscatter Observations on the GLOBE Pacific Survey Missions." Seventh Symposium on Meteorological Observations and Instrumentation: Special Sessions on Laser Atmospheric Studies, American Meteorological Society, New Orleans, LA, pp. J261 – J264, 14-18 January 1991.

30. Srivastava, V., Clarke, A.D., Porter, J., Jarzembski, M. and Bowdle, D. "Comparison of CO_2 Backscatter using Mei Theory from Aerosol Measurements over Pacific Basin with Lidar Data," Seventh Symposium on Meteorological Observations and Instrumentation: Special Sessions on Laser Atmospheric Studies, American Meteorological Society, New Orleans, LA, pp. J268 – J271, 14-18 January 1991.

31. Targ, R., et al. "Coherent lidar airborne windshear sensor: performance evaluation," Applied Optics, Vol. 30, No. 15, pp. 2013-2026, 20 May 1991.

32. Targ, R., et al. "Coherent lidar airborne wind sensor II: flight-test results at 2 and 10μm," Applied Optics, Vol. 35, No. 36, pp. 7117-7127, 20 December 1996.

33. Thomson, J.A., Huffaker, R.M. and Richmond, R.D. "2 micron coherent laser radar for on-board aircraft vortex wake detection: pattern recognition techniques and technology assessment," *From proceedings of a conference on wake vortex detection organized by Volpe about eight years ago.*

34. Wallace, J.M. and Hobbs, P.V. Atmospheric Science: An Introductory Survey, Academic Press, Inc., 1977.

35. Zrnic, D.S. "Estimation of spectral moments for weather echoes," IEEE Transactions on Geoscience Electronics, Vol. GE-17, No. 4, pp. 113-128, October 1979.

36. "American National Standard for the Safe Use of Lasers," American National Standards Institute, ANSI Z136.1-1993, February 1993.

37. "Manufacturers See Evolutionary Change to Handle Turbulence," Aviation Week & Space Technology, pp. 76 – 79, 27 July 1998.

38. "Method for the Calculation of the Absorption of Sound by the Atmosphere," American National Standards Institute, ANSI S1.26-1995, July 1995.